AGU PUBLICATIONS

JGR

Journal of Geophysical Research: Oceans

RESEARCH ARTICLE

10.1002/2016JC012251

Key Points:
- There is strong correspondence between observed ice type and independently estimated frequency-dependent wave dissipation rate
- The dissipation versus frequency profiles do not exhibit the "roll-over" effect reported in some prior observational and theoretical studies
- Cases with pancakes in frazil with visual indicators for thicker ice cover have highest dissipation rate, particularly at high frequencies

Supporting Information:
- Supporting Information S1
- Figure S1
- Figure S2
- Data Set S1
- Table S1
- Movie S1

Correspondence to:
W. E. Rogers,
erick.rogers@nrlssc.navy.mil

Citation:
Rogers, W. E., J. Thomson, H. H. Shen, M. J. Doble, P. Wadhams, and S. Cheng (2016), Dissipation of wind waves by pancake and frazil ice in the autumn Beaufort Sea, *J. Geophys. Res. Oceans*, *121*, doi:10.1002/2016JC012251.

Received 17 AUG 2016
Accepted 10 OCT 2016
Accepted article online 13 OCT 2016

Dissipation of wind waves by pancake and frazil ice in the autumn Beaufort Sea

W. Erick Rogers[1], Jim Thomson[2], Hayley H. Shen[3], Martin J. Doble[4], Peter Wadhams[5], and Sukun Cheng[3]

[1]Naval Research Laboratory, Stennis Space Center, Mississippi, USA, [2]Applied Physics Laboratory, University of Washington, Seattle, Washington, USA, [3]Department of Civil and Environmental Engineering, Clarkson University, Potsdam, New York, USA, [4]Polar Scientific Ltd., Argyll, UK, [5]Department of Applied Mathematics and Theoretical Physics, University of Cambridge, Cambridge, UK

Abstract A model for wind-generated surface gravity waves, WAVEWATCH III®, is used to analyze and interpret buoy measurements of wave spectra. The model is applied to a hindcast of a wave event in sea ice in the western Arctic, 11–14 October 2015, for which extensive buoy and ship-borne measurements were made during a research cruise. The model, which uses a viscoelastic parameterization to represent the impact of sea ice on the waves, is found to have good skill—after calibration of the effective viscosity—for prediction of total energy, but over-predicts dissipation of high frequency energy by the sea ice. This shortcoming motivates detailed analysis of the apparent dissipation rate. A new inversion method is applied to yield, for each buoy spectrum, the inferred dissipation rate as a function of wave frequency. For 102 of the measured wave spectra, visual observations of the sea ice were available from buoy-mounted cameras, and ice categories (primarily for varying forms of pancake and frazil ice) are assigned to each based on the photographs. When comparing the inversion-derived dissipation profiles against the independently derived ice categories, there is remarkable correspondence, with clear sorting of dissipation profiles into groups of similar ice type. These profiles are largely monotonic: they do not exhibit the "roll-over" that has been found at high frequencies in some previous observational studies.

1. Introduction

In the eastern Siberian, Chukchi, and western Beaufort Seas, the ice season duration is shrinking at a rate of no less than 23 days every 10 years [*Stammerjohn et al*., 2012], and in the Chukchi and Beaufort Seas, the trend in delay of ice advance is 1.4 days per year [*Thomson et al*., 2016a]. This has motivated research studies to determine the implications, including those for short and medium-range prediction of the marine environment [atmosphere, surface waves, ice coverage, ocean circulation]. The interactions between these four components—as well as adjacent land—include both positive and negative feedback mechanisms that have implications for the longer time scales. For example, a wind/wave event may fracture and accelerate the melting of the ice, and the retreat of the ice would make available more fetch for generation of more wave energy during the next wind/wave event, a positive feedback [*Thomson and Rogers*, 2014]. Or, a wave event may cause upward mixing of heat stored in the ocean, facilitating the venting of heat to the atmosphere, which again has implications for subsequent ice growth and melt.

The present paper contributes to the topic of frequency-dependent dissipation of waves by sea ice; specifically, pancake and frazil ice. While dissipation and scattering by ice generally has seen significant attention in the literature [e.g., *Wadhams et al*., 1988; *Squire et al*., 1995], in situ field measurement of waves in pancake and frazil ice is much more rare [e.g., *Wadhams et al*., 1996, 2004; *Doble et al*., 2015]. Frazil ice is composed of needle-shaped ice crystals, and aggregates in slurries near the water surface. Thinner slurries tend to be a dark color, often the same color as the open water, or slightly lighter, but with a much smoother appearance due to absence of capillary waves; this is known as "grease ice." Under calm conditions, given time, this thin layer will tend to freeze into new sheet ice (nilas). Under weak-to-moderate wave action, it instead aggregates into rounded miniature floes known as pancakes, with shape and size controlled by accumulation, bending, and collisions under the wave action [*Shen et al*., 2001]. Under stronger wave action, the outer edges become raised from these collisions, often with a lighter, frosted appearance. Strong wave

action also acts to inhibit the adhesion of frazil to the pancakes, which results in accumulation of a thicker frazil layer with a lighter, "slushy" appearance. All of these ice types dissipate wave energy, with higher frequency energy typically experiencing the highest rate of dissipation [e.g., *Wadhams et al*., 1988; *Squire et al*., 1995]. As the wave conditions become calm—either in time, as the driving winds decline, or in space, as the waves propagate further from the open sea into the ice—the pancakes will tend to freeze in place, forming consolidated pancake ice, essentially sheet ice with small ridges. An apparent common theme to the above is that the ice formation and wave action are inextricably linked, or in the parlance of modeling, "nonlinearly two-way coupled." Further, the above assumes water temperature and salinity are conducive to ice formation: introduction of saltier water or warmer temperatures may reverse any of these processes. Lastly, winds and surface currents will tend to compress or dilate the sea ice [e.g., *Doble*, 2009]. The outcome is a highly nonstationary and nonuniform environment that is a significant challenge for anyone seeking to describe (or predict) it using a numerical model.

The variability described above also presents a challenge when interpreting in situ observations. The compression and dilation of ice in the case of *Doble* [2009] led to distinct regimes in the inferred dissipation characteristics. In separate experiments by the present authors using moored, upward-looking wave measurements (the same data set as used by *Thomson and Rogers* [2014]), the dissipation rate could be estimated as the Marginal Ice Zone (MIZ) advanced and retreated past the mooring, but it was not possible to connect this with the ice type, except in the most generic sense, e.g., "an ice cover during retreat." This absence of ice information hinders future application of the knowledge gained in a predictive model. In the present paper, this limitation is addressed by using photographs of the ice, taken by the same buoys used to measure the wave conditions.

Another challenge is the estimation of the dependence of dissipation on wave frequency. The most common approach is to deploy an array of sensors and compute dissipation rate from the differences in measured wave energy, accounting for the direction of wave propagation [e.g., *Wadhams et al*., 1988. *Kohout et al*., 2014; *Doble et al*., 2015]. This method treats wave energy as unforced (i.e. swell), which raises obvious concerns when there is the possibility of generation (or regeneration) of wave energy between instruments, either by wind or by nonlinear transfer processes. The problem tends to be greater when studying higher frequencies (e.g., 0.2 to 0.5 Hz), which may contribute to the common—but likely often spurious—"roll-over" effect in which dissipation rate has a nonmonotonic dependence on frequency in observational data. This problem is discussed by *Wadhams et al*. [1988] and *De Carolis and Desiderio* [2002]. In the present study, a nontraditional approach is used: the dissipation rate is estimated by an inversion technique that involves applications of a spectral wave model, WAVEWATCH III® ("WW3") [*Tolman and the WAVEWATCH III® Development Group*, 2014] that include the process of generation by wind and some nonlinear transfers. The method produces an estimate of dissipation to the frequency limit of the buoys (0.49 Hz) and does not give a high-frequency roll-over effect, spurious or otherwise, in our experiments. The model-based approach of course has its own shortcomings relative to the conventional method, as will be discussed herein.

This paper is structured as follows: in section 2, the numerical model is described, including its representations of the effects of sea ice. In section 3, the observational experiment and model hindcast are described. In section 4, forward model results and the inversion method and results are given. Inferred frequency-dependent dissipation rate is presented for several different groupings of ice types. For pancakes in frazil ice, the dissipation profiles are interpreted in the context of a visco-elastic model available in WW3. Sections 5 and 6 contain discussions and conclusions.

2. Sea Ice in WAVEWATCH III

The WAVEWATCH III® model (henceforth denoted "WW3") [*Tolman* 1991, *Tolman and the WAVEWATCH III® Development Group*, 2014] is a phase-averaged model for wind-generated surface gravity waves based on the radiative transfer equation. In this approach, the dependent variable is the wave spectrum (denoted E for wave energy spectral density or N for wave action spectral density), which is a function of wavenumber or frequency (k or σ), direction (θ), space (x,y), and time (t), with spectral density most commonly defined on frequency and direction. The left hand side of the radiative transfer equation includes terms for time rate of change and propagation, while the right hand side includes source functions (dynamics):

$$\frac{\partial N}{\partial t}+\nabla\cdot\vec{c}N=\frac{S}{\sigma} \quad (1)$$

where $\vec{c}$ describes the propagation velocities in x, y, k, and θ, e.g., in absence of currents, c_x is the x-component of group velocity C_g. The sum of all source functions is denoted as S, and individual source functions are denoted with appropriate subscript, for example, dissipation by whitecapping is S_{wc}, and dissipation by ice is S_{ice}. For more detailed description of the model, we refer the reader to *Tolman and the WAVEWATCH III® Development Group* [2014].

The present paper is not intended as a review or general evaluation of the treatment of sea ice in WW3, and more complete descriptions have been published previously. As such, the following paragraphs describe this treatment only briefly. Taken together, that collaborative body of work is the first S_{ice} implementation in any open-source community model suitable for routine global and regional forecasting (WW3). However, the concept of S_{ice} in a phase-averaged wave model is not new [e.g., *Komen et al*. 1994] and has been implemented in at least one other large-scale wave model [*Doble and Bidlot*, 2013], as well as other, more specialized models [e.g., *Kohout and Meylan*, 2008; *Dumont et al*., 2011; *Williams et al*., 2013a,2013b; *Bennetts et al*., 2014].

2.1. Dissipation

Historically, sea ice was treated in phase-averaged wave models by simplistic methods. In WW3 version 1 [*Tolman*, 1997] and WAM Cycle 4 [*Komen et al*., 1994], sea ice was treated as either open water or land, with the binary selection being based on ice concentration (the fraction of the surface covered by ice). This was updated by *Tolman* [2003] to a "continuous treatment" to allow partial blocking for partial ice cover. These methods do not treat the effect as "dissipation" via the S_{ice} term, but rather as a feature of the propagation scheme. Further, they do not permit variation of dissipation rate with frequency. In WW3, these methods are variants of what is denoted as the "IC0" method. *Rogers and Orzech* [2013] implemented a simple alternative that introduces the S_{ice} term. This method is denoted as "IC1," and here the imaginary portion of the complex wavenumber k_i is specified by the user, representing the exponential decay rate of amplitude in space. This input parameter is still uniform in frequency, but allowed to vary in time and space. It is related to the temporal decay rate of energy D_{ice} by $D_{ice}=-2C_g k_i$, and to S_{ice} by $S_{ice}=D_{ice}E$. *Rogers and Orzech* [2013] also introduced the scheme of *Liu et al*. [1991], which assumes that dissipation is caused by turbulence at the ice-water interface, represented by a phenomenological eddy viscosity parameter. This method is denoted as "IC2" and does predict variation with frequency. The "IC3" scheme was added to WW3 by *Rogers and Zieger* [2014], implementing the model of *Wang and Shen* [2010], a generalized continuum model that treats the ice as a viscoelastic layer. Required inputs for IC3 are ice concentration, thickness, density, effective viscosity, and effective modulus of elasticity. All three S_{ice} schemes were available in the version 4 public release of WW3 [*Tolman and the WAVEWATCH III® Development Group*, 2014], and improvements have been made by the WW3 community since, e.g., IC2 has since been updated to optionally replace the eddy viscosity scheme with a boundary layer parameterization (by F. Ardhuin (Ifremer) and applied in *Ardhuin et al*. [2016]) and IC3 has been optimized for faster computations. Though primary documentation exists only in the nonpeer-reviewed literature (references above), the IC3 feature of WW3 has already been applied in the peer-reviewed literature [*Li et al*., 2015; *Wang et al*., 2016].

2.2. Scattering

Dissipative effects described above are nonconservative modes of wave attenuation. In the MIZ, waves can also be attenuated by the conservative processes of reflection and scattering (redistribution of energy within the spectral directional distribution). These processes are not considered in the present study, since the floe sizes encountered (up to 2 m but usually less than 1 m) are small relative to the wavelengths considered and are not expected to produce significant scattering [e.g., *Komen et al*., 1994, *Dumont et al*., 2011, *Bennetts and Squire*, 2012]. At time of writing, scattering by ice is included in the development version of WW3 [e.g., *Ardhuin et al*., 2016], with plans to include it in a forthcoming public release (version 5).

2.3. Refraction and Shoaling (Real Part of Wavenumber)

Both IC2 and IC3 are based on computations of the complex wavenumber using dispersion relations which asymptote to the open water dispersion relation as appropriate, e.g., as ice thickness approaches zero. As noted above, the imaginary part of the complex wavenumber, k_i, provides the dissipation rate. The real part

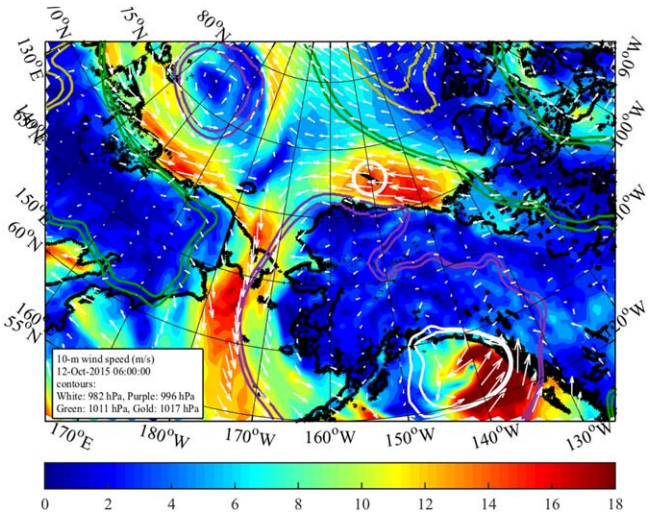

Figure 1. 10 m winds speeds (color scaling) and directions (arrows) from meteorological model NAVGEM: nowcast for 0000 UTC 12 October 2015. Contours of pressure at mean sea level are colored as follows: white: 982 hPa; purple: 996 hPa; green: 1011 hPa; gold: 1017 hPa. The white circle bisected by a black line indicates the study area and experimental transect of the 11–14 October wave experiment.

of the complex wavenumber, k_r, is the traditional wavenumber which indicates physical wavelength, $L=2\pi/k_r$. This ice-modified wavenumber also provides an ice-modified group velocity, $C_{g,ice}=\partial\sigma/\partial k_r$. Modifications to k_r and C_g produce effects analogous to refraction and shoaling (respectively) by bathymetry. These effects were implemented for IC3 by *Rogers and Zieger* [2014], with details given in *Tolman et al.* [2014]. This feature remains experimental.

2.4. Scaling of Open-Water Source Functions

Following *Komen et al.* [1994] and *Perrie and Hu* [1996], WW3 (version 4 and later) modifies the source function S_{in} and the deepwater breaking (whitecapping) source function S_{wc} by the open water fraction:

$$S_{in(\text{in ice})}=(1-C)S_{in(\text{in open water})} \tag{2}$$

$$S_{wc(\text{in ice})}=(1-C)S_{wc(\text{in open water})} \tag{3}$$

where C is the ice concentration. The source term for four-wave nonlinear interactions, S_{nl4}, is not modified, following *Perrie and Hu* [1996]. A lack of dissipation by whitecapping in full ice cover is a natural assumption. The situation with respect to wind input is less obvious. The treatment of S_{in} implies that if ice concentration is 100%, the wind-to-wave energy flux is completely shut down, even if the ice is merely a thin layer of grease ice. We regard this as a probable source of error, and this issue is explored in section 5 and the supporting information.

3. Wave Experiment and Hindcast Design

A large number of observational studies were conducted during a six-week research cruise on the *R/V Sikuliaq* during the autumn of 2015 in the Chukchi Sea, western Beaufort Sea, and the neighboring areas of the Arctic Ocean. The general goal of this cruise was to study the implications of reduced ice cover for the dynamic interactions between the atmosphere, ice, ocean and waves [*Thomson*, 2015; *Wadhams and Thomson*, 2015]. Though the research cruise was conducted during the seasonal ice advance, this advance was episodic, and included periods of ice retreat. One such retreat occurred during a wave event 11–14 October 2015, and this event was the subject of the wave experiment used in the present study.

3.1. Meteorological Conditions

The meteorological conditions which produced the wave event are summarized in Figure 1, a graphic created using data from a NAVGEM (Navy Global Environmental Model) [*Hogan et al.*, 2014] nowcast run at the Fleet Numerical Meteorology and Oceanography Center (FNMOC). A high pressure system existed to the north of the study area, producing easterly and southeasterly winds in the Beaufort Sea. There was also a low pressure system south of the study area with a center in the Gulf of Alaska. NAVGEM gives the lowest pressure of this system as 962 to 964 hPa from 1200 to 2100 UTC 11 October 2015. The counter-rotation of this second system may have also contributed to the strong winds in the Beaufort Sea (see the 996 hPa isobar in Figure 1). According to the model, 10 m wind speeds reached 23 m/s east of study area (1500 UTC 11 October) and up to 16 m/s within the study area (0600 UTC 12 October). Figure 1 also indicates the location of the wave experiment.

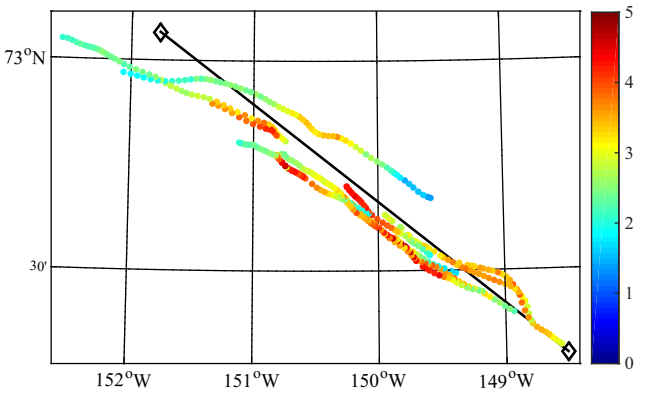

Figure 2. H_{m0} values (in meters) computed from hourly spectra, 0600 UTC 11 October to 0800 UTC 14 October 2015 from 11 SWIFT and Doble/Wadhams buoys. A black line indicates the nominal transect, 137.2 km in length.

3.2. Measurements

The wave experiment was located at the western edge of the Beaufort Sea and the adjacent Arctic Ocean. Starting on 0600 UTC 11 October 2015, drifting buoys were deployed from the *R/V Sikuliaq* along a transect with two design features: First, the azimuth coincided with the expected dominant wave direction: these were from the southeast, at 125° (meteorological convention). Second, the southeast terminus of the transect coincided with the initial ice edge, so that the entire transect was initially covered with ice in high concentration (50 to 100%), and the region southeast of the transect was open water according to contemporary SAR (Synthetic Aperture Radar) imagery. The buoys drifted at 0.2 to 1.0 m/s toward the northwest during the experiment (Figure 2). The last buoy used in this study was recovered at 0800 UTC 14 October, and the ship remained in the vicinity of the transect until 2100 UTC.

Numerous observational data were collected from the ship and satellites during the wave experiment, including atmospheric boundary layer flux measurements, marine radar, LiDAR (Light Detection and Ranging), physical ice sampling, visual ice observations (logged using formal protocols), photography, and underway CTD (Conductivity, Temperature, Depth). The reader is referred to *Wadhams and Thomson* [2015] for additional description. The present article focuses on data collected by drifting buoys. Four types of buoys were used during the wave event, and we focus here on those which recorded waves along the transect described above, which were of two types. The first is the spar-shaped SWIFT (Surface Wave Instrument Float with Tracking) buoy [*Thomson*, 2012], each equipped with an anemometer, Acoustic Doppler Current Profiler (ADCP), GPS receiver, radio and satellite transmitters, a low-power camera system, and an inertial measurement unit (IMU). Six SWIFT buoys were deployed along the transect, denoted here as buoys S09, S11, S12, S13, S14, and S15. The second type of buoy was designed, engineered, and operated by coauthor MD in collaboration with coauthor PW, both of whom participated in the experiment. These buoys are referred to as "UK buoys" by *Wadhams and Thomson* [2015] and are referred to as Doble/Wadhams buoys here, with shorthand notation for individual buoys as D02, D03, D04, D05, and D07. These buoys included a phase-resolving GPS compass, IMU and satellite transmission of GPS position for recovery. Five of these buoys were deployed along the transect. For these 11 buoys, true displacement time series were calculated from the buoy IMUs, which was then used to compute the spectra of sea surface elevation variance. In a prior experiment during the same cruise, the two buoy types were cross-checked to verify that they provide consistent results. Directional information is available from all buoys, but this is not utilized in the present study.

When the present analysis was performed, the SWIFT spectral data were available at 10- or 12 min intervals and those from the Doble/Wadhams buoys were available at 15 min intervals. These were colocated in time by performing simple time-averaging of available spectra to the zero-minute time at the top of each hour. It is noted that reprocessing and time-averaging of spectra does have an impact on the extremes in the time series [*Gemmrich et al.*, 2016]. For example, for S09, using the preliminary processing based on GPS measurements of horizontal orbital velocities [*Herbers et al.*, 2012] with 10 min intervals, the maximum $H_{m0}=5.40$ m; after reprocessing using true heave with 10 min intervals, the maximum $H_{m0}=4.84$ m; and after averaging to one record per hour, the maximum $H_{m0}=3.97$ m. Peak periods during the experiment were typically close to 10 seconds (median=9.7 s and standard deviation=0.9 s). Figure 2 illustrates the transect and H_{m0} values computed from the hourly spectra. In total, 403 hourly buoy spectra were processed for use in subsequent analysis.

Serial cameras mounted on the masts of the SWIFT buoys recorded a low-resolution (320 by 240 pixels) image every 5 seconds during 512 second-long bursts, at intervals of 600 seconds (i.e., a duty cycle

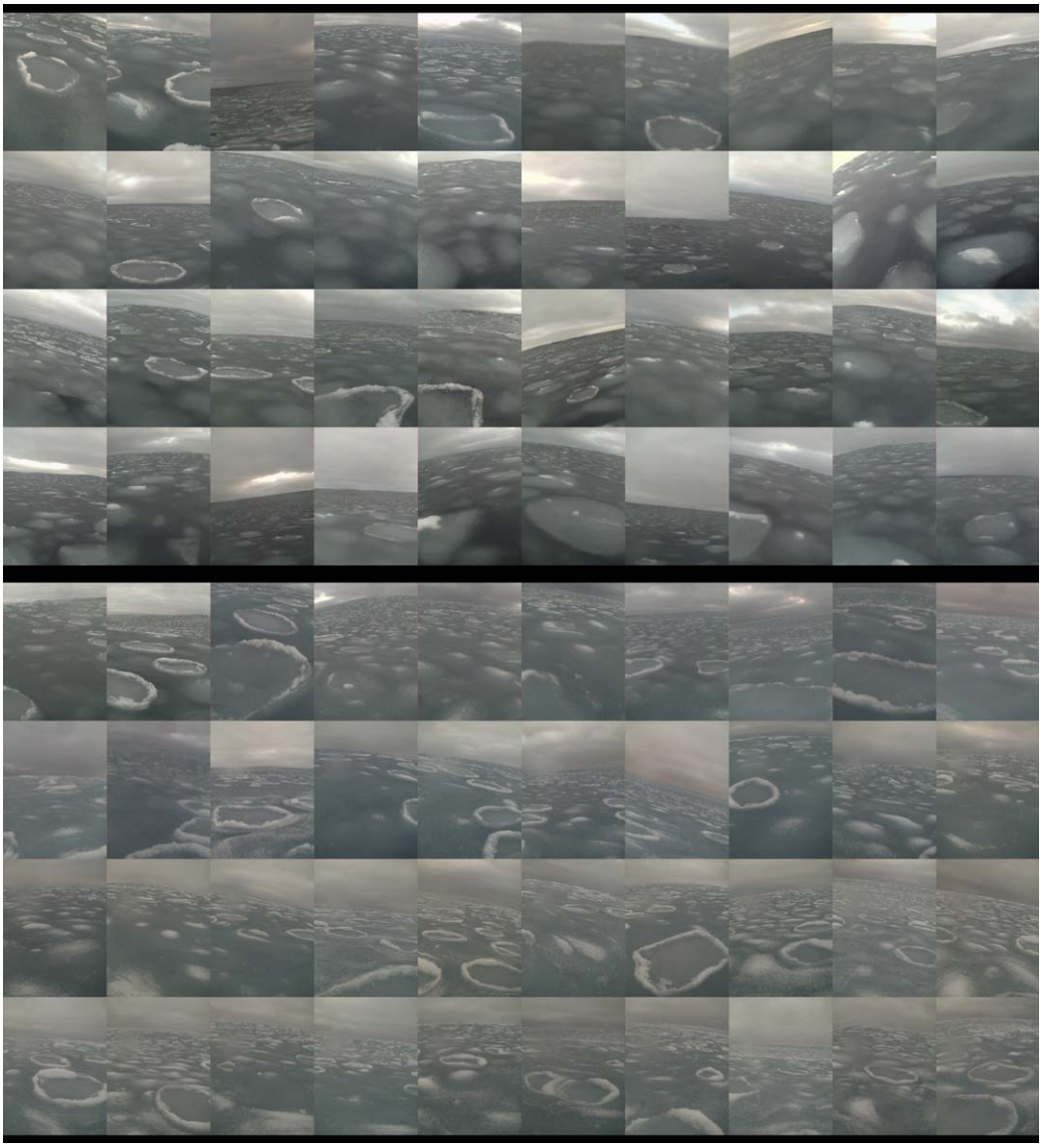

Figure 3. Example SWIFT photos. All correspond to ice code for pancakes in frazil (and nonblurry). Upper panel corresponds to smaller inferred dissipation rate of high frequency wave energy, relative to lower panel with larger dissipation rate. Inferred dissipation rate is explained and this figure is further discussed in section 4. The bottom edge of each photo spans approximately 65 cm when the buoy is in neutral position (e.g., not tilting).

sampling for 512 seconds and processing for 48 seconds). These were organized into a database of 444 1 h sets of approximately 525 photographs each, and each set was subsampled to a more manageable 105 photographs each. Each set represents minutes 0 to 59.99 for each hour, and is thus centered at 30 minutes after the hour, and so is offset from its corresponding hourly buoy spectrum by 30 minutes. Each set was inspected—or if obviously unusable, then discarded—by the author (ER) and subjectively assigned an integer code to designate the observed ice conditions, e.g., open water, mixed open water and grease ice, or pancakes and frazil. These integer codes are listed in Appendix A, and for clarity are denoted with more intuitive designations within the figures here, e.g., "P/FR" for "pancakes in frazil." Most sets were unusable due to darkness or icing of the camera, and many were only partially usable due to partial icing (and thus blurring) of the images; information about this blurring is contained in the integer codes. In the end, 102 sets were found to be usable or partially usable, and so there are 102 matched pairs of ice codes and one-dimensional buoy spectra. Each of the 102 sets was subsequently subsampled to 50 images each and combined into 5×10 mosaics. (These are available with the supporting information.) Figure 3 shows examples

of SWIFT photographs, all corresponding to the ice code denoting "pancakes in frazil" (P/FR). Unlike the 5× 10 mosaics, the two mosaics in Figure 3 each contain images from multiple times and buoys (randomly selected, but all with the P/FR ice code).

3.3. Hindcast Design

One unconventional feature of the *R/V Sikuliaq* cruise was that experimental plans were developed and refined on daily basis by the Chief Scientist (author JT), in consultation with the Science Team and crew. This planning utilized new information from satellite (primarily SAR imagery of ice, but also passive microwave radiometry), meteorological forecasts, and wave forecasts. The wave forecasting consisted of 1) on-ship wave model runs using forcing fields of ice and winds delivered by ftp to the ship and 2) plots from shore-based wave model runs, also delivered by ftp. In the former case, WAVEWATCH III (introduced in section 2) was used, and the simulations were run on a laptop computer, so the computational grid design needed to be frugal with computer resources. A two-grid system was used; both were irregular grids, which is a useful feature at high latitudes where regular latitude/longitude grids are inefficient with respect to Courant–Friedrichs–Lewy (CFL) stability limits. The same two-grid system is applied in the hindcasts presented here.

The grids are illustrated in the supporting information. The outer grid is a polar stereographic projection grid with grid spacing of 15 km. Active grid points include longitudes from 90°E to 270°E, thus including eastern Siberia and Canada but excluding Greenland, the Nordic Seas, and western Siberia. Swell energy propagating through the central ice pack for the latter areas is assumed to be small and neglected. The maximum latitude is 89°N and the southern limit is south of St. Lawrence Island in the northern Bering Sea. While the Bering Sea is a very active region for wave generation, this island effectively blocks most energy that would otherwise propagate north through the narrow (82 km) Bering Strait: this wave energy is assumed to be small and neglected here. Boundary forcing in the form of directional wave spectra are passed from the outer grid to inner grid via a traditional one-way nesting approach. The inner grid is an irregular grid with a central meridian at Barrow, Alaska, and grid lines formed by tracing great circles west and east from the central meridian, starting from points at 10 km intervals on the meridian, with grid points at 10 km intervals along the great circles.

For the hindcast, the numerical wave model WW3 is again used. For open water, the physics package of *Ardhuin et al*. [2010] is used. The spectral grid includes 36 directional bins and 31 frequency bins (0.0418 to 0.73 Hz, logarithmically spaced). The physics package of *Ardhuin et al*. [2010] requires specification of a parameter, $\beta_{\max}$ which is used to compensate for the mean bias of the input wind fields, or lack thereof; the default setting of $\beta_{\max}=1.52$ is used for these hindcasts. This setting was judged to be suitable based on comparison of total wave energy to a buoy moored in open water to the west of the study area (this is the "Acoustic Wave And Current" (AWAC) mooring described in *Wadhams and Thomson* [2015]).

Hindcasts are performed for 15 September to 15 November 2015, but of course, only the period of 11–14 October is of interest here. Wind forcing in the form of 10 m wind vectors comes from archives of the operational NAVGEM (introduced in section 3.1), concatenating nowcasts and short-term forecasts at 3 hourly intervals (forecast time $\tau=0$ to 9 hours). Description of the treatment of ice in the outer grid is omitted here for sake of brevity, since all the damping of waves by sea ice relevant to the present analysis occurs within the inner grid. Ice concentration and thickness for that grid is taken from a 2 km regional implementation of the Los Alamos Community Ice Code (CICE) [*Hunke and Lipscomb*, 2008]. *Hebert et al*. [2015] describe a comparable, but larger scale, implementation of this system. The 2 km model was designed and operated by Dr. Hebert (U.S. Naval Research Laboratory) specifically for support of the summer and autumn cruises of the *USCG Healy* and the cruise of the present study (*R/V Sikuliaq*). In the hindcasts presented here, concatenated analysis fields are used, prescribed at 24 hourly intervals.

For dissipation of wave energy by ice, the viscoelastic continuum model of *Wang and Shen* [2010] implemented in WW3 as "IC3" is used in the forward model hindcast (section 3), based on the belief that such a model is more physically appropriate for the ice cover encountered (primarily loose pancakes and frazil ice), versus the "turbulence under ice" model or scattering model which are also implemented in WW3 (section 2). The effective viscosity parameter is set as $\nu=0.03$ m^2/s as a gross calibration to minimize bias relative to buoy measurements of total energy, without regard to spectral shape. The effective elasticity G is set to

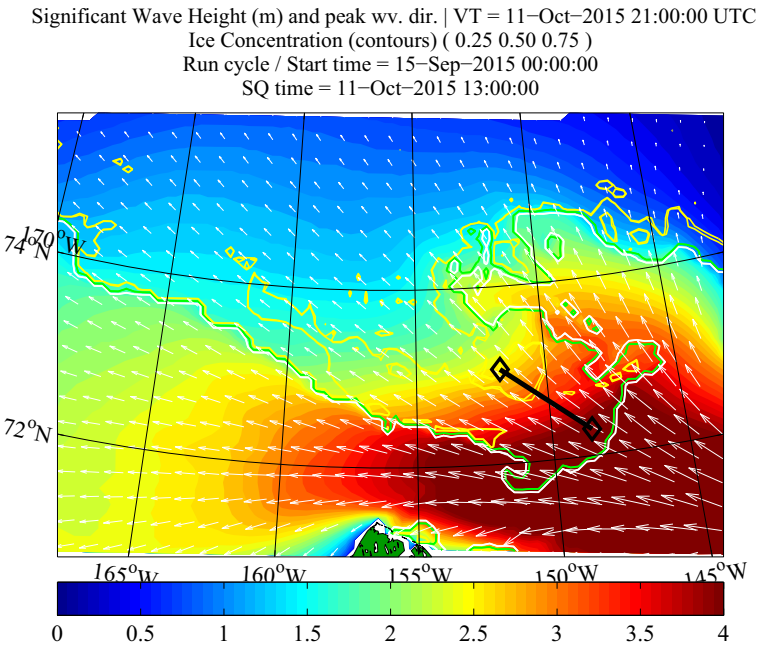

Figure 4. An example plot from the baseline model, for 2100 UTC 11 October 2015. Colors indicate significant waveheight (m). Arrows indicate mean wave direction at spectral peak. Contours indicate ice concentration (25%, 50%, and 75%). Black line indicates transect of wave experiment, as shown in Figure 2.

zero under the presumption that elasticity of loose pancake and frazil ice is minimal. These selections are revisited in section 4.

The experimental WW3 features producing refraction and "shoaling" by ice are not included in this hindcast, or other simulations herein. With ν=0.03 m^2/s and G=0 as used here, the impact would have been minor if included; for example, with an ice thickness of 40 cm (a relatively high value for this hindcast) and considering waves at 0.35 Hz (one of the more strongly affected wave frequencies measurable by buoy), the ice changes the group velocity by less than 1% of the open water group velocity, according to the *Wang and Shen* [2010] model. However, such behavior is not universal among viscoelastic models [*Mosig et al.*, 2015].

4. Results

Results are presented in two parts: in section 4.1, we analyze the hindcast introduced in section 3.3 using buoy data introduced in section 3.2. In section 4.2, we apply a new inversion procedure which uses a simpler representation of ice in WW3 and buoy wave observations to estimate the frequency distribution of dissipation rate, $k_i(f)$ corresponding to each measured wave spectrum.

4.1. Hindcast (Forward Model)

Figure 4 shows an example result from the baseline hindcast described in section 3. Wave directions are well aligned with the azimuth of the transect. According to this model, the largest significant waveheights occurred between 1500 UTC 11 October and 0300 UTC 12 October, with values up to 4.2 m within the transect and up to 5.2 m south and east of the transect. Peak periods were close to 10 seconds, consistent with the buoy observations (at buoy locations, median=10.1 s and standard deviation=0.7 s).

Wave spectra are output from WW3 at computational grid points that bound each of the 403 hourly buoy observations, and are bi-linearly interpolated to the buoy positions during post-processing. For our analysis, we use two parameters, significant waveheight $H_{m0}=4\sqrt{m_0}$, and the spectral moment m_4, where $m_n=\int E(f)f^n df$, $E(f)$ is the spectral density of sea surface variance in m^2/Hz, and f is frequency in Hz. H_{m0} is used to evaluate the model's ability to predict total energy, which is dominated by the so-called "energy-containing" region near the spectral peak; it is thus largely insensitive to the spectral tail. Sea ice is expected to have a stronger influence on higher frequencies [e.g., *Wadhams et al.*, 1988] than on frequencies at the

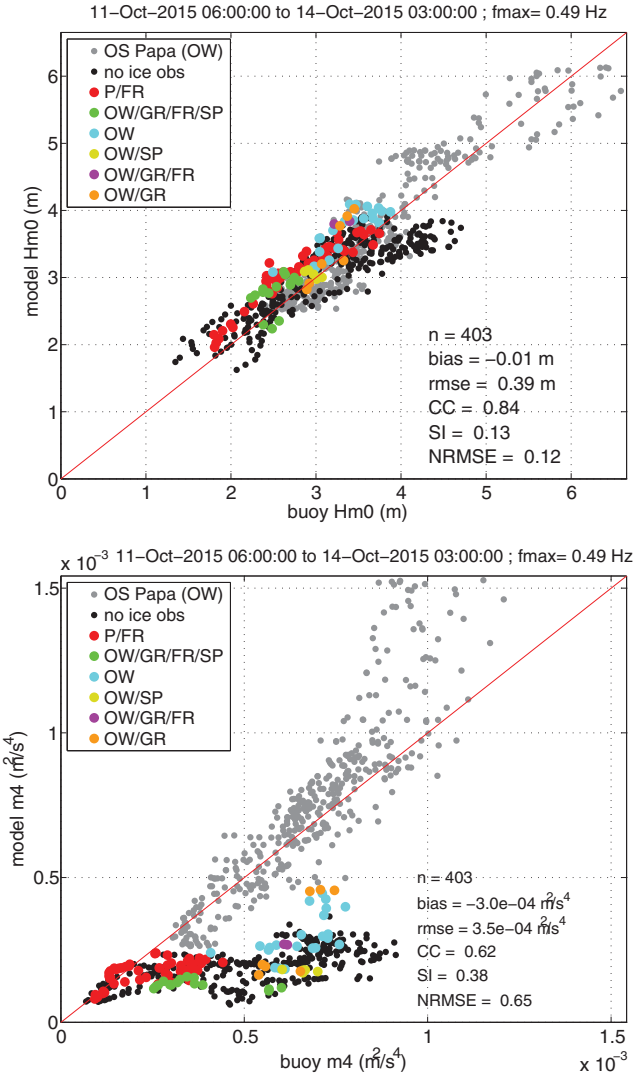

Figure 5. (top) Scatter plot of H_{m0}. (bottom) scatter plot of m_4. Both plots include color coding for ice conditions: see Appendix A for ice type designations. Gray points are for a separate hindcast in open water (see main text), and are not included in statistics shown, which are: bias, RMS error, correlation coefficient, scatter index, and normalized RMS error. Definitions are given in the Appendix B.

peak, so the parameter m_4, being strongly weighted by higher frequencies, is an appropriate parameter for the present study. (NB: to provide it with a physical meaning: m_4 is proportional to the mean square slope of the water surface, which is dominated by shorter wind-waves, e.g., frequencies greater than 0.2 Hz in this case).

The baseline hindcast is evaluated using scatter plots of these two parameters in Figure 5. For the 102 SWIFT spectra with corresponding ice observations, the points are color-coded by ice type. To provide a reference, scatter points are also included for a separate hindcast that is in open water but otherwise comparable to the present hindcast. This is from a deployment of SWIFT buoys near Ocean Station Papa in the north Pacific during January 2015 [*Thomson et al.*, 2016b]. Additional description of the Papa wave hindcast can be found in the supporting information. A consistent maximum frequency is used for integration of the spectral parameters: 0.49 Hz.

The comparison suggests that while significant waveheight is predicted with a level of skill that is acceptable in context of the challenging environment (e.g., RMS error is 39 cm, only moderately higher than the RMS error for the Papa hindcast, which was 32 cm), m_4 is poorly predicted (e.g., normalized RMS error of 0.65). In the case of H_{m0}, there is less grouping by ice type: for example, while ice designation OW/GR (open water and grease ice) occupy a narrow range in the plot, ice designation P/FR (pancakes in frazil) includes a wider range, with H_{m0} values from 1.8 to 3.8 m. In the case of m_4, there is strong grouping by ice type. The m_4 parameter is almost universally under-predicted by the hindcast, except for a subset (30 to 40%) of the P/FR cases. This indicates that the model is strongly damping high frequency energy in all cases, while the buoys indicate that this strong damping is occurring only for that subset of cases. This is illustrated further in Figure 6, which is a comparison of 1-d spectra for three SWIFT buoys, corresponding to identical times (2200 UTC 12 October), but different locations. In this case, S09 (solid red line) is coded as "open water and possible grease ice and very sparse pancakes," and shows a high frequency tail that is not unlike that typically seen in open water. S14 (solid blue line), coded as "pancakes and frazil" shows a strongly damped tail, and S15 (solid green line), coded as "mixed open water, frazil and brash pancakes," indicates an intermediate level of damping of the tail. The model, as with Figure 5, always indicates high damping of the tail, comparable to that evident in the spectrum measured by buoy S14, but markedly different from that of S09 and S15. This situation is almost certainly associated with model's input ice fields (e.g., Figure 4), which do not capture the localized thinning or opening of the ice cover evident in the photographs. In the S14 comparison in Figure 6, at 0.4 Hz, there is underprediction of energy by the model that cannot be ascribed to the ice

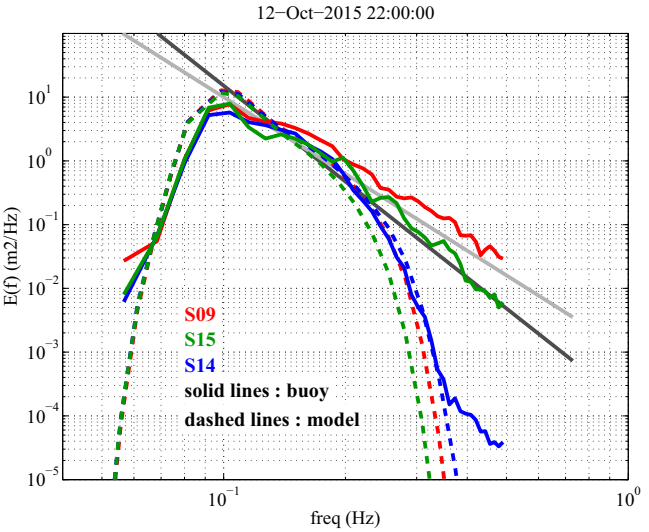

Figure 6. Example comparisons of 1-d spectrum, for three different SWIFT buoys, corresponding to the same time (2200 UTC 12 October). Dark and light gray lines correspond to an f^{-5} and f^{-4} tail slope, respectively. Solid red, dark green, and blue lines are measured spectra. Corresponding dashed lines are from the model hindcast.

forcing. It may be associated with overprediction of dissipation by the IC3 physics, or measurement error (e.g., noise).

4.2. Estimated Dissipation Rate (Inverse Model)

Herein, we quantify dissipation rate using k_i, the exponential decay rate of amplitude in space, introduced in section 2. This variable is expected to depend on ice rheology and wave frequency. To put our estimates in context, it is useful to consider other examples. *Doble et al.* [2015] found k_i values up to approximately 7×10^{-4} m^{-1} in pancake ice near Antarctica, for waves of 8 second period, with values for thinner pancake being significantly smaller, e.g., 1×10^{-4} m^{-1}. The reader is referred to other articles for examples of attenuation rate in non-pancake floes: *Wadhams et al.* [1988], *Liu et al.* [1991], and *Meylan et al.* [2014]. In these articles, the quantity is most correctly termed "attenuation rate" as opposed to "dissipation rate," since some observed attenuation is a result of nondissipative scattering. Also, the reader should keep in mind that these articles present the energy decay rate α, which is twice the amplitude decay rate, $\alpha=2k_i$.

From section 4.1, we found that while H_{m0} predictive skill is generally acceptable, that of m_4 is not, and in the context of the latter we can conclude that observed ice conditions are a useful predictor for the skill of the forward model. Application of the same rheological parameters ($\nu=0.03$ m^2s^{-1}, $G = 0$) with the given ice forcing—thick ice (15 to 45 cm) in high concentration (50 to 100%)—only yields acceptable m_4 results for some observed ice types, and only a subset of those. This being the case, we take a different tack in the present section. We temporarily set aside the physics-based IC3 model, determine the optimal dissipation profile $k_i(f)$ that provides a match to the each buoy spectrum, and evaluate the outcome in context of observed ice type. Subsequently, the results are compared with the IC3 model dissipation profiles, thus bringing the model physics back into the discussion.

The basic concept of a model inversion process is to determine the model inputs that will produce a particular model output. Loosely defined, the gross calibration of the viscosity parameter ν to produce small bias in waveheight is a crude form of inversion. Similarly, if elasticity parameter G is found to significantly influence bias in another wave parameter (say, m_4), then a two-parameter (two input, two output) calibration can be performed. However, the term "model inversion" is more commonly used to label more complex analyses.

One approach (not used here) is to apply a forward model repeatedly for each of 17 fixed k_i values using the IC1 method described in section 2. Then, for each frequency, the k_i that produces the least bias for energy at that frequency is selected. The end result is a step-wise description of $k_i(f)$ that represents the time period used to calculate the bias. Though this method provides a concise outcome, it sacrifices information about temporal variability.

The approach used here is similar to the prior insofar as the model is run for many different fixed k_i values. It differs insofar as an optimal $k_i(f)$ distribution is calculated for *each* buoy spectrum. For each spectrum and for each frequency bin, we determine the optimal k_i, where $E_{obs}(f)=E_{model}(f)$. The buoy and model spectra are first preconditioned by organizing into eight coarse frequency bins centered at 0.075, 0.120, 0.175, 0.225, 0.275, 0.325, 0.375, and 0.445 Hz, which increases the degrees of freedom of the spectra with the intent of providing more reliable results [e.g., *Elgar*, 1987]. As the spectra are now colocated in time,

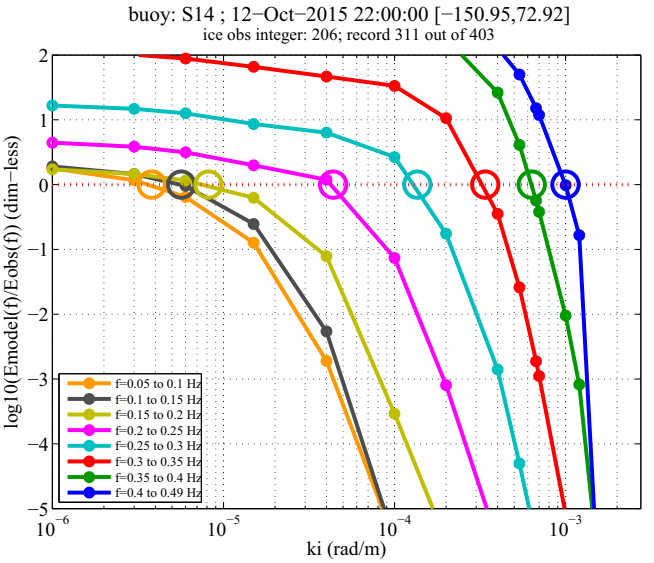

Figure 7. Example of the inversion process, corresponding to a single measured spectrum (S14, 2200 UTC 12 October). A zero on vertical axis corresponds to "optimal value" of k_i (circles), determined by linear interpolation from model versus observation comparisons (dots). Each discrete value on the horizontal axis corresponds to a separate simulation (13 are visible here, out of 17 used). Each curve corresponds to a frequency interval of the spectrum (see Legend).

space, and frequency, the inversion is simply a minimization process for $|log_{10}(E_{model}(f)/E_{obs}(f))|$, as illustrated in Figure 7. The end result is the dissipation profile $k_i(f)$ for each buoy spectrum.

This method does have limitations that must be mentioned. First, dissipation is not instantaneous, but is rather an integrated effect. This implies that the $k_i(f)$ includes the effect on the wave spectrum of ice at previous times, and other (up-wave) locations, and it must be recognized that this ice is variable in time and space. Second, there is an assumption of linearity, specifically that the solution for optimal k_i at one frequency is not affected by use of nonoptimal k_i at neighboring frequencies in the same "fixed k_i" simulation. However, recognizing that nonlinear interactions do exist in the model, the validity of this assumption is discussed further in section 5. Third, the inversion, like the forward model, does depend on the accuracy of the forcing provided to it. The inversion, unlike the baseline model, is not dependent on the accuracy of the ice thickness fields since ice thickness is not used, but it does depend on the accuracy of the ice concentration fields, since the S_{ice} source function is scaled with ice concentration (section 2). For example, if the input concentration is biased high, the inversion will compensate by reporting a lower k_i. Fourth, the inversion, like the forward model, depends on the accuracy of the wave model. As mentioned in section 2, we have particular concerns about the assumption that wind input scales with the fraction of open water. This is discussed in section 5, and the analysis is repeated with an alternate assumption.

Results from the inversion are shown in Figure 8. Each line corresponds to one of the 403 buoy spectra, and each colored line corresponds to one of the 102 SWIFT spectra with valid ice observation. There is a clear grouping by ice type. Though this is an intuitive outcome, it is an encouraging result, especially considering that the ice categories and k_i profiles are arrived at by completely independent methods. In fact, if these 102 sets are sorted by the dissipation rate at the 7th (of 8) frequency bins, 100% of the first 53 values are coded as "pancakes and frazil" (P/FR, red lines in Figure 8) while none of the remaining 52 values have this code, a remarkable correspondence. A column-sortable spreadsheet is provided with the supporting information to demonstrate this.

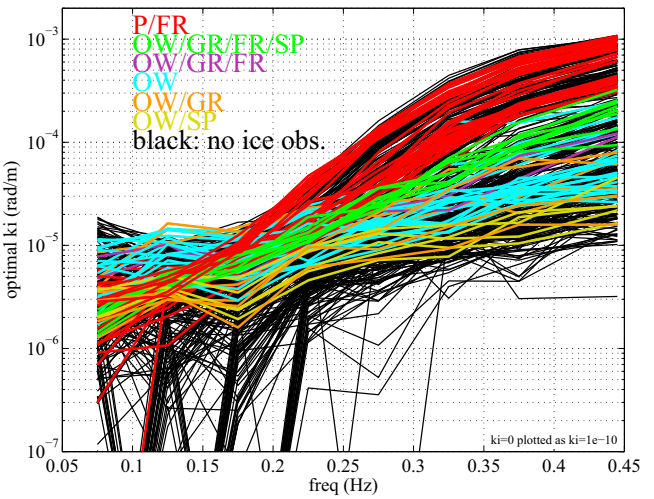

Figure 8. Profiles of dissipation rate k_i with frequency f. Cases with valid ice observation are color-coded by ice type.

It is, of course, unsurprising that of the ice types observed in the experiment, the "pancakes and frazil" sets have the highest estimated dissipation rates.

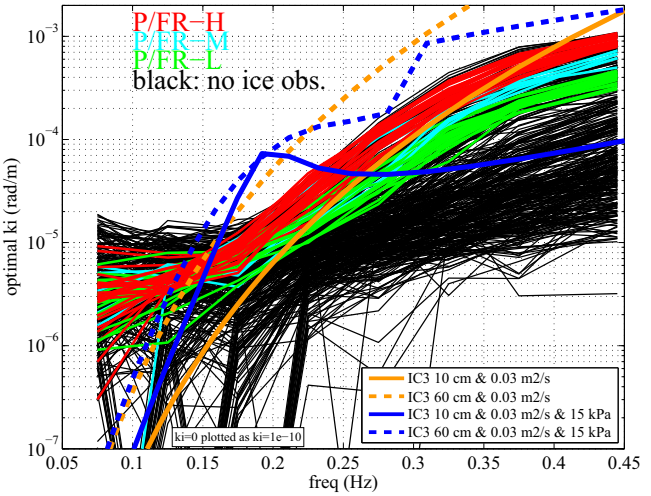

Figure 9. Similar to Figure 8, except only color-coding the "code P/FR" cases, and separating into three subgroups, P/FR-H (red), P/FR-M (cyan), and P/FR-L (light green). Dissipation profiles from simple application of the *Wang and Shen* [2010] model are shown in orange (without elasticity) and blue (with elasticity), with two ice thickness values (solid: 10 cm; dashed: 60 cm)

Analysis of wave buoy data in the Antarctic has shown that wave attenuation (hence dissipation) can be directly scaled with pancake and frazil ice thickness [*Doble et al.*, 2015]. Of the cases with mixed open water, grease, and frazil, the cases with brash pancakes have higher dissipation rate (i.e. green lines are higher than the purple lines), which is again quite intuitive. However, there are some features of the results that are not intuitive. For example, there are 22 cases with "open water" (cyan lines), and these are *not* the lowest dissipation values. This is most likely associated with the fact that, while the photos are local in nature, the k_i is determined via integration in time and space (i.e. nonlocal), as discussed above.

None of the dissipation profiles indicate a clear "roll-over effect" [e.g., *Liu et al.*, 1991; *Squire et al.*, 1995], where dissipation at high frequencies is less than that of middle frequencies.

At the high-frequency end of Figure 8, there is a noticeable separation of the P/FR ice types (red lines) into three subgroups. To look at this feature further, the comparison is repeated in Figure 9, but only the P/FR are color-coded, and these three subgroups are identified with "H," "M," and "L," for high, medium and low dissipation rate. This leads to an obvious question: do these three groupings—based on comparison of model and observed spectra—correspond with differences in the appearance of the ice? In other words, could the original visual classification as "pancakes and frazil" have included subcategories? In upper panel of Figure 3, the mosaic is composed of SWIFT photos corresponding to P/FR-L, and in lower panel of Figure 3, to P/FR-H. Each is composed of randomly selected nonblurry photos from the category. The most noticeable difference between the two mosaics is the coloration of the regions between the subaerial pancakes: in the P/FR-L photos, these regions are usually darker, suggesting thinner frazil ice. Much of these regions in the P/FR-H photos have a "frosted" appearance indicating small areas where water has drained from the ice: this is attributed to a deep underlying frazil ice suspension, which has sufficient buoyancy to lift the topmost ice crystals clear of the water surface. Also, though both mosaics contain both subaerial and submerged pancakes, the subaerial pancakes constitute a larger fraction in the P/FR-H mosaic.

Figure 9 is also used to compare with IC3 dissipation profiles with fixed rheology: these are computed with simple application of the S_{ice} module, and are independent of the hindcast. The orange lines correspond to a S_{ice} that treats the ice as a viscous layer, as with the baseline hindcast of section 4.1, for two ice thickness values. The steepness of the curves $\partial k_i/\partial f$ is noticeably greater than that implied by the inversion process. When S_{ice} instead treats the ice as a viscous-elastic layer (blue lines), this steepness is reduced. However, we notice in this case, some erratic behavior in $k_i(f)$, which is almost certainly associated with the model's selection of a solution from among multiple solutions available (i.e. "root selection"). This concern has been raised already by *Mosig et al.* [2015], and is a priority for future improvement of the IC3 module. Nevertheless, the comparison suggests an IC3 with elasticity may be better able to match the inversion-based dissipation profiles than a model without elasticity.

5. Discussion

As mentioned in Section 4.2, the assumption of linearity in the inversion process is a matter of concern. In essence, it is assumed that the dissipation rate at one frequency does not affect the calculation of optimal dissipation rate at another frequency. This was tested by applying the forward model with a S_{ice} that is a

simple step function based on the averages of the P/FR-H dissipation profiles, and similar for P/FR-L. The biases of the resulting frequency distributions of energy were acceptably low in most cases. However, with P/FR-L, there was a slight negative bias in the 0.10 to 0.20 Hz range, and with P/FR-H, there was a consistent modest negative bias in the 0.15 to 0.20 Hz range, e.g., buoy *E(f)* is 1.0 m^2/Hz where the model has 0.8 m^2/Hz. This indicates that a nonlinear (and thus more exact) inversion would result in slightly weaker dissipation at this band. From this analysis we believe that the nonlinear coupling between frequencies does not affect the k_i curves significantly in our case. These comparisons are included in the supporting information.

The above, considered with the outcome of section 4.2, suggests that if the ice type is known, e.g., "pancakes and thick frazil" or "pancakes and thin frazil," the model can be applied with a parametric ice-appropriate step function of $k_i(f)$. We assert, however, that a more physics-based approach—applying IC3 with an ice-appropriate rheology which fits that step function—is better, since it requires fewer free parameters and uses a continuous treatment of the ice thicknesses available from the ice model, rather than just "thick" or "thin." Either method, of course, requires accurate input, which is the greatest challenge presently. New methods need to be developed for prediction of ice type from satellite data and ice model output. Further, results here indicate that capturing the spatial and temporal variability of the ice cover is crucial. However, to do this deterministically is far beyond the capability of present-day ice modeling. A probabilistic approach is a more practical next step.

As mentioned in sections 3 and 4, the baseline model uses concentration and thickness from the CICE model, and inversion uses the concentration. Both are applied at the wave model's 10 km resolution. Though we have not conducted detailed analysis, it is worthwhile to share our general impressions of the accuracy of these fields. The ice concentration from the analysis was typically 50 to 80% over the buoy array, with a decreasing trend during the wave event. Concentrations reported by visual observers included all possible values (0 to 100%), but this is not necessarily inconsistent with the model, taken in context of spatial and temporal averaging. SAR imagery suggests marked retreat of the ice edge (e.g., 60 km by 1700 UTC 12 October), only partially represented in the ice analysis. A "post mortem" evaluation of the ice product during 11–14 October indicates that the overprediction of the ice cover is associated with assimilation of fields from the National Ice Center's Ice Mapping System [*Helfrich et al*., 2007] that had not been updated in this area for the period of 12–14 October, thereby missing the ice retreat. Ice thickness values from the analysis were 5 to 45 cm over the buoy array. Actual values are difficult to estimate, but we regard thicknesses less than 25 cm to be more credible, based on our interpretation of direct measurement of samples collected by coauthor PW and Mr. Robin Clancy (Cambridge University).

Another uncertainty in the inversion, as briefly mentioned in section 4.2, is the accuracy of the model itself, and a major concern is the assumption that the wind input source function scales with the fraction of open water. It is generally agreed [e.g., *Hristov et al*., 2003, and references therein] that the transfer of momentum from atmosphere to the waves occurs through normal rather than tangential stresses. Thus, we hypothesize that in case of loose ice cover, where the floes are small relative to the wavelength, or if the ice cover is otherwise flexible, momentum may be transferred through the ice cover to the waves. We have plans to study this problem using observational data, but for the present study, we must regard it as unknown. Having already applied the model with one assumption (zero wind input with 100% ice cover), we repeat the analysis with an opposing assumption: full wind input regardless of ice cover. Recognizing that reality should be somewhere between these two extremes, these paired analyses bound our problem and quantify the maximum level of uncertainty in our results associated with this issue. The inversion outcome analogous to that shown in Figure 8 is shown here, as Figure 10. The result indicates that this treatment of wind input has insignificant impact on relative dissipation rate, but does have a major quantitative impact. The dissipation curves here are more tightly grouped. This is caused by strongly increased dissipation rate for the less dissipative cases (e.g., k_i for OW/GR and OW/SP are increased by an order of magnitude), while the more dissipative cases (P/FR) are increased by a much smaller amount (e.g., less than a factor of two). This is understood simply to imply that the introduction or enhancement of wind input has a proportionately stronger impact on the source term balance when the source term total is small (i.e. weakly dissipative ice cover).

The assumption made regarding the dependence of wave breaking on ice cover is of lesser concern, since there were no reliable observations—either from the ship, or via SWIFT camera—of breakers in regions of significant ice cover; in other words, we have no reason to suspect that this assumption is wrong.

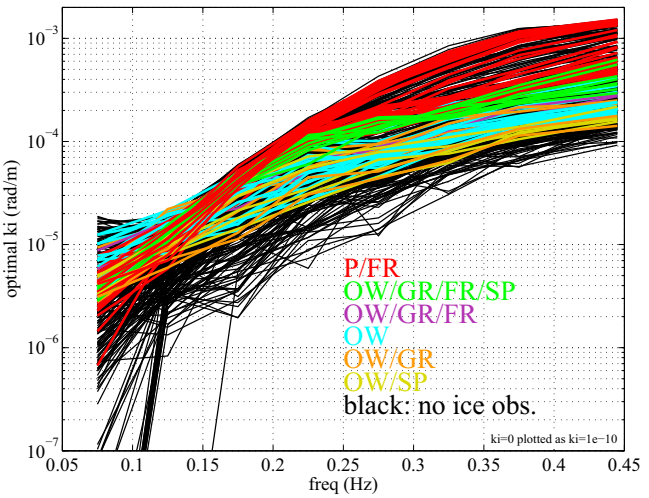

Figure 10. Similar to Figure 8, but produced assuming that the wind input source function is unaffected by ice cover.

As noted in section 2, we run the wave model such that the traditional four-wave nonlinear interactions that occur in open water, S_{nl4}, are not modified by ice, following *Perrie and Hu* [1996]. Descriptions in *Masson and LeBlond* [1989], *Komen et al.* [1994], and *Doble and Bidlot* [2013] imply that they used the same approach. The rationale behind this approach is difficult to determine. *Doble and Bidlot* [2013] cite *Polnikov and Lavrenov* [2007, hereinafter "PL07"], stating that S_{nl4} "can be used" in ice-covered seas, which is a strictly correct reading of PL07, but does not fully address the scaling issue. *Williams et al.* [2013a] cite PL07 for confirming that S_{nl4} is the same in ice-covered seas, which unambiguously addresses the scaling issue. *Lavrenov* [2003] states that S_{nl4} is "qualitatively the same" in ice, and PL07 say essentially the same thing. However, PL07 conclude that the intensity of nonlinear transfers *decreases* as ice thickness increases. In other words, S_{nl4} is not *quantitatively* the same in ice cover, and requires scaling or other modification. *Lavrenov* [2003, in his section 7.4] earlier made a similar conclusion, though his comparison (his Figure 7.3) did not actually isolate the relevant effect. Further, he notes that ice causes an *increase* in energy flow to high frequencies. Clearly, the question of how to treat S_{nl4} in ice cover within models such as WW3 should not be considered as yet "resolved."

An uncertainty exists in the use of photos for interpreting the inversion results: these photos are local in scope, so for example, a buoy may be in an isolated patch of open water that is not representative of the larger region. This may explain why the inversion indicates nonzero damping in cases where the photos indicate open water.

6. Conclusions and Recommendations

6.1. Conclusions

This study involves two main components: (1) a hindcast with the WAVEWATCH III (WW3) model, using the *Wang and Shen* [2010] visco-elastic model (denoted as "IC3 model") for dissipation of wave energy by sea ice, and (2) a new inversion procedure which uses a simpler form of WW3 and buoy wave observations to estimate the frequency distribution of dissipation rate, $k_i(f)$ corresponding to each measured wave spectrum. Both are applied to a wave dataset from the Beaufort Sea and western Arctic Ocean, collected in October 2015. Results are interpreted using photographs of ice conditions taken by the wave buoys.

With respect to (1), we find that while the total energy is predicted with acceptable accuracy, the hindcast overpredicts the dissipation of high frequency wave energy for a large majority of cases. The extent of the overprediction is clearly associated with observed ice conditions. Regions of thin or sparse ice cover are under-represented in the forcing used, and this contributes significantly to the overprediction of high frequency dissipation.

From (2), we find the following:

1. There is strong correspondence between observed ice type and the dissipation profiles $k_i(f)$ estimated independently by the inversion process. The correspondence is clearest at higher frequencies, where dissipation is strongest.
2. The dissipation profiles $k_i(f)$ are largely monotonic, without the "roll-over" effect reported in some prior observational and theoretical studies. We concur with previous authors who suggest that this may be a spurious feature in the prior observational studies.

3. The cases identified as "pancakes in frazil" using the buoy photos exhibit dissipation profiles in three distinct groupings. It is found that the group with highest dissipation at high frequencies corresponds to cases that have visual indicators for thicker ice cover, and for the group with lower dissipation, the reverse is true.
4. The inversion-based dissipation rates $k_i(f)$ have a $\partial k_i/\partial f$ less steep than that of the viscosity-only variant of the IC3 model, though simple computations suggest that the steepness of the IC3 $\partial k_i/\partial f$ may be lowered to better match that of the inversion profiles by prescribing a nonzero elasticity.

6.2. Recommendations

Though significant works remains for modeling of waves in sea ice, e.g., with respect to wave scattering and reflection, much progress has been made recently to adapt operationally used codes such as WAVEWATCH III and WAM for this purpose. For example, the dissipation profiles $k_i(f)$ estimated herein can, in principle, be used to determine optimal rheological parameters for wave hindcasts where ice type is known to be similar to those observed in this wave experiment. Conversely, without knowledge of ice type, these dissipation profiles have limited utility. We believe that the most serious challenge in this endeavor during the next decade will be the provision of accurate information to the wave model about ice characteristics—something which of course is itself often affected by the wave conditions—and we recommend new uses of ice modeling and satellite data to advance this capability.

Lastly, we believe that the uncertainty regarding the impact of sea ice cover on atmosphere-to-wave momentum flux is a problem that urgently needs to be addressed, as highlighted by our demonstration that estimated dissipation rates are sensitive to this uncertainty.

Appendix A: Ice Codes

As noted in the main text, hourly groups of SWIFT photos were assigned integer codes to identify ice type. This was done during the cruise, prior to any hindcasts. During preparation of the manuscript, these codes were organized into groups for purposes of color-coding figures, and assigned letter identifiers, for ease of discussion:

1. P/FR: Pancakes in frazil, as in Figure 3. Integer code=206. Frazil is primarily thick, but pancakes with grease ice are also included here.
2. OW/GR/FR/SP: Integer codes 104, 106, 107. Sparse pancakes or pancake debris (brash) in either a) mixed open water and frazil, or b) frazil.
3. OW/GR/FR: Integer codes 004. No pancakes, with some mixure of open water and frazil.
4. OW: Integer codes 000 and 001. Open water. Includes cases of "possible" grease ice, where it is difficult to distinguish open water from grease ice due to photo quality.
5. OW/GR: Integer codes 002, 003, 102. Mix of open water and grease ice. Includes cases of "probable" grease ice, where it is difficult to distinguish open water from grease ice due to photo quality.
6. OW/SP: Integer code 101. Same as "OW," but with very sparse pancake wreckage (brash).

Note that frazil can be one of two types:

1. thin frazil (a.k.a. grease ice), or
2. thick frazil, which has a lighter "slushy" appearance .

Appendix B: Error Metrics

In the main text, five statistics used to quantify accuracy are:

1. bias, i.e. the mean error.
2. root-mean-square error (RMSE).
3. Pearson's correlation coefficient (CC) as computed by, for example, *Cardone et al.* [1996] and *Ardhuin et al.* [2010], $\mathrm{CC}=\frac{\langle(O-\bar{O})(M-\bar{M})\rangle}{\sqrt{\langle(O-\bar{O})^2\rangle}\sqrt{\langle(M-\bar{M})^2\rangle}}$, where $\bar{}$ and $\langle\rangle$ indicate a mean, O are observations and M are model values.
4. scatter index SI, the standard deviation of errors divided by the mean of observations.
5. normalized root-mean-square error, as given by *Ardhuin et al.* [2010], $\mathrm{NRMSE}=\sqrt{\frac{\sum(O-M)^2}{\sum O^2}}$.

Acknowledgments
We wish to thank the UW engineers Joe Talbert and Alex DeKlerk and UW graduate student Madison Smith for their substantial labors building, preparing, maintaining, deploying and recovering the SWIFT buoys, and managing the associated data. We gratefully acknowledge the support of the crew of the *R/V Sikuliaq* and the ship's marine technicians. Fabrice Ardhuin (Ifremer) contributed important WW3 code that was used in the hindcast. David Hebert (NRL) performed the CICE analysis used as forcing for WAVEWATCH III herein. Luigi Cavaleri (CNR-ISMAR), Pamela Posey (NRL), Tripp Collins (NRL), and an anonymous reviewer provided useful comments on a draft of this manuscript. We thank the Sea State team for numerous discussions and tutoring on varied topics. Model output presented here can be obtained from the corresponding author by request. WAVEWATCH III is an open-source model code, with public releases occurring every two to four years, and specific, relevant routines can be obtained earlier from the corresponding author by request. SWIFT buoy data are available at apl.uw.edu/swift. Some data are provided with this paper, including tabulated parameters and mosaics of buoy photos (see supporting information). This work was supported by the Office of Naval Research Code 322, "Arctic and Global Prediction," directed by Martin Jeffries and Scott Harper. Grants: *Doble*: N000141310290; Rogers: N0001413WX20825; *Shen*: N000141310294; and *Thomson*: N000141310284. This is NRL contribution NRL/JA/7320-2016-3153 and is approved for public release.

References

Ardhuin, F., et al. (2010), Semi-empirical dissipation source functions for ocean waves: Part I, definitions, calibration and validations, *J. Phys. Oceanogr.*, *40*, 1917–1941.

Ardhuin, F., P. Sutherland, M. Doble, and P. Wadhams (2016), Ocean waves across the Arctic: Attenuation due to dissipation dominates over scattering for periods longer than 19 s, *Geophys. Res. Lett.*, *43*, 5775–5783, doi:10.1002/2016GL068204.

Bennetts, L. G., and V. A. Squire (2012), On the calculation of an attenuation coefficient for transects of ice-covered ocean, *Proc. R. Soc. A*, *468*(2137), 136–162, doi:10.1098/rspa.2011.0155.

Bennetts, L. G., S. O'Farrell, P. Uotila, and V. A. Squire (2014), Towards a model of the marginal ice zone for use in climate studies, in *Proceedings of the 22nd IAHR International Symposium on Ice*, 7 pp., International Association for Hydro-environment Engineering and Research (IAHR), Singapore.

Cardone, V. J., R. E. Jensen, D. T. Resio, V. R. Swail, and A.T. Cox (1996), Evaluation of contemporary ocean wave models in rare extreme events: the "Halloween Storm" of October 1991 and the "Storm of the Century" of March 1993, *J. Atmos. Oceanic Technol.*, *13*, 198–230.

De Carolis, G., and D. Desiderio (2002), Dispersion and attenuation of gravity waves in ice: a two-layer viscous model with experimental data validation, *Phys. Lett. A*, *305*, 399–412.

Doble, M. J. (2009), Simulating pancake and frazil ice growth in the Weddell Sea: A process model from freezing to consolidation, *J. Geophys. Res.*, *114*, C09003, doi: 10.1029/2008JC004935.

Doble, M. J., and J.-R. Bidlot (2013), Wavebuoy measurements at the Antarctic sea ice edge compared with an enhanced ECMWF WAM: progress towards global waves-in-ice modeling, *Ocean Modell.*, *70*, 166–173, doi:10.1016/j.ocemod.2013.05.012.

Doble, M. J., G. De Carolis, M. H. Meylan, J.-R. Bidlot, and P. Wadhams (2015), Relating wave attenuation to pancake ice thickness, using field measurements and model results, *Geophys. Res. Lett.*, *42*, 4473–4481, doi:10.1002/2015GL063628.

Dumont, D., A. Kohout, and L. Bertino (2011), A wave-based model for the marginal ice zone including a floe breaking parameterization, *J. Geophys. Res.*, *116*, C04001, doi:10.1029/2010JC006682.

Elgar, S. (1987), Bias of effective degrees of freedom of a spectrum, *J. Waterw. Port Coastal Ocean Eng.*, *113(1)*, 77–82.

Gemmrich, J., J. Thomson, W. E. Rogers, A. Pleskachevsky and S. Lehner (2016), Spatial characteristics of ocean surface waves, *Ocean Dyn.*, *66*, 1025–1035, doi:10.1007/s10236-016-0967-6.

Hebert, D. A., R. A. Allard, E. J. Metzger, P. G. Posey, R. H. Preller, A. J. Wallcraft, M. W. Phelps, and O. M. Smedstad (2015), Short-term sea ice forecasting: An assessment of ice concentration and ice drift forecasts using the U.S. Navy's Arctic Cap Nowcast/Forecast System, *J. Geophys. Res. Oceans*, *120*, 8327–8345, doi:10.1002/2015JC011283.

Helfrich, S. R., D. McNamara, B. H. Ramsay, T. Baldwin, and T. Kasheta (2007), Enhancements to, and forthcoming developments in the Interactive Multisensor Snow and Ice Mapping System (IMS), *Hydrol. Processes*, *21*, 1576–1586.

Herbers, T. H. C., P. F. Jessen, T. T. Janssen, D. B. Colbert, and J. H. Macmahan (2012), Observing ocean surface waves with GPS tracked buoys, *J. Atmos. Oceanic Technol.*, *29*, 944–959, doi:10.1175/JTECH-D-11-00128.1.

Hogan, T., et al. (2014), The Navy Global Environmental Model, *Oceanography*, *27(3)*, 116–125.

Hristov, T. S., S. D. Miller, and C. A. Friehe (2003), Dynamical coupling of wind and ocean waves through wave-induced air flow, *Nature*, *422*, 55–58.

Hunke, E. C. and W. H. Lipscomb (2008), CICE: The Los Alamos Sea Ice Model. Documentation and software user's manual. Version 4.0, *Tech. Rep. LA-CC-06-012*, T-3 Fluid Dyn. Group, Los Alamos Natl. Lab.

Kohout, A. L., and M. H. Meylan (2008), An elastic plate model for wave attenuation and ice floe breaking in the marginal ice zone, *J. Geophy. Res.*, *113*, C09016, doi:10.1029/2007JC004434.

Kohout, A. L., M. J. M. Williams, S. M. Dean, and M. H. Meylan (2014), Storm-induced sea-ice breakup and the implications for ice extent, *Nature*, *509*, 604–607.

Komen, G. J., L. Cavaleri, M. Donelan, K. Hasselmann, S. Hasselmann, and P. A. E. M. Janssen (1994), *Dynamics and Modelling of Ocean Waves*, 532 pp., Cambridge Univ. Press, Cambridge, U. K.

Lavrenov, I. V. (2003), *Wind-Waves in Ocean*, 386 pp., Springer, Berlin.

Li, J., A. L. Kohout, and H. H. Shen (2015), Comparison of wave propagation through ice covers in calm and storm conditions, *Geophys. Res. Lett. 42*, 5935–5941, doi:10.1002/2015GL064715.

Liu, A. K., B. Holt, and P. W. Vachon (1991), Wave propagation in the Marginal Ice Zone: Model predictions and comparisons with buoy and Synthetic Aperture Radar data, *J. Geophys. Res.*, *96*, 4605–4621.

Masson, D., and P. H. LeBlond (1989), Spectral evolution of wind-generated surface gravity waves in a dispersed ice field, *J. Fluid Mech.*, *202*, 43–81.

Meylan, M., L. G. Bennetts, and A. L. Kohout (2014), In situ measurements and analysis of ocean waves in the Antarctic marginal ice zone, *Geophys. Res. Lett.*, *41*, 5046–5051, doi:10.1002/2014GL060809.

Mosig, J. E. M., F. Montiel, and V. A. Squire (2015), Comparison of viscoelastic-type models for ocean wave attenuation in ice-covered seas, *J. Geophys. Res. Oceans*, *120*, 6072–6090, doi:10.1002/2015JC010881.

Perrie, W., and Y. Hu (1996), Air-ice-ocean momentum exchange. Part I: Energy transfer between waves and ice floes, *J. Phys. Oceanogr.*, *26*, 1705–1720.

Polnikov, V.G. and I.V. Lavrenov (2007), Calculation of the nonlinear energy transfer through the wave spectrum at the sea surface covered with broken ice, *Oceanology*, *47*(3), 334–343.

Rogers, W. E., and M. D. Orzech (2013), Implementation and testing of ice and mud source functions in WAVEWATCH III®, *NRL Memo. Rep. NRL/MR/7320-13-9462*, 31 pp., Naval Research Laboratory, Washington, D. C.

Rogers, W. E., and S. Zieger (2014), New wave-ice interaction physics in WAVEWATCH III®, in *Proceedings of 22nd IAHR International Symposium on Ice*, 8 pp., International Association for Hydro-environment Engineering and Research (IAHR), Singapore.

Shen, H. H., S. F. Ackley, and M. A. Hopkins (2001), A conceptual model for pancake-ice formation in a wave field, *Ann. Glaciol.*, *33*, 361–367.

Squire, V. A., J. P. Dugan, P. Wadhams, P. J. Rottier, and A. K. Liu (1995), Of ocean waves and sea ice, *Annu. Rev. Fluid Mech.*, *27*, 115–168.

Stammerjohn, S., R. Massom, D. Rind, and D. Martinson (2012), Regions of rapid sea ice change: An inter- hemispheric seasonal comparison, *Geophys. Res. Lett.*, *39*, L06501, doi:10.1029/2012GL050874.

Thomson, J. (2012), Wave breaking dissipation observed with SWIFT drifters, *J. Atmos. Oceanic Technol.*, *29*, 1866–1882, doi:10.1175/JTECH-D-12-00018.1.

Thomson, J. (2015), ONR Sea State DRI Cruise Report: R/V Sikuliaq, Fall 2015 (SKQ201512S), 45 pp., University of Washington, Seattle, Wash. [Available at http://www.apl.washington.edu/project/project.php?id=arctic_sea_state, last accessed 9 Aug. 2016.]

Thomson, J., and W. E. Rogers (2014), Swell and sea in the emerging Arctic Ocean, *Geophys. Res. Lett.*, *41*, 3136–3140, doi:10.1002/2014GL059983.

Thomson, J., et al. (2016a), Emerging trends in the sea state of the Beaufort and Chukchi seas, *Ocean Modell.*, *105*, 1–12, doi:10.1016/j.ocemod.2016.02.009.

Thomson, J., M. S. Schwendeman, S. F. Zippel, S. Moghimi, J. Gemmrich, and W. E. Rogers (2016b), Wave-breaking turbulence in the ocean surface layer, *J. Phys. Oceanogr.*, *46*, 1857–1870, doi:10.1175/JPO-D-15-0130.1.

Tolman, H. L. (1991), A Third generation model for wind-waves on slowly varying, unsteady, and inhomogeneous depths and currents, *J. Phys. Oceanogr.*, *21(6)*, 782–797.

Tolman, H. L. (1997), User manual and system documentation of WAVEWATCH-III version 1.15, *Tech. Note 151 NOAA/NWS/NCEP/MMAB*, 104 pp., National Centers for Environmental Prediction, Camp Springs, Md.

Tolman, H. L. (2003), Treatment of unresolved islands and ice in wind wave models, *Ocean Modell.*, *5*, 219–231.

Tolman, H. L. and the WAVEWATCH III® Development Group (2014), User Manual and System Documentation of WAVEWATCH III® version 4.18, *Tech. Note 316, NOAA/NWS/NCEP/MMAB*, 282 pp. + Appendices, National Centers for Environmental Prediction, College Park, Md.

Wadhams, P., and J. Thomson (2015), The Arctic Ocean cruise of R/V Sikuliaq 2015, An investigation of waves and the advancing ice edge, *Il Polo, LXX-4*, 9–38.

Wadhams, P., V. A. Squire, D. J. Goodman, A. M. Cowan, and S. C. Moore (1988), The attenuation rates of ocean waves in the marginal ice zone, *J. Geophys. Res.*, *93*, 6799–6818.

Wadhams, P., J. C. Comiso, E. Prussen, S. Wells, M. Brandon, E. Aldworth, T. Viehoff, R. Allegrino and D. R. Crane (1996), The development of the Odden ice tongue in the Greenland Sea during winter 1993 from remote sensing and field observations, *J. Geophys. Res.*, *101*, 18,213–18,235.

Wadhams, P., F. F. Parmiggiani, G. de Carolis, D. Desiderio, and M. J. Doble (2004), SAR imaging of wave dispersion in Antarctic pancake ice and its use in measuring ice thickness, *Geophys. Res. Lett.*, *31*, L15305, doi:10.1029/2004GL020340.

Wang, R., and H. H. Shen (2010), Gravity waves propagating into an ice-covered ocean: A viscoelastic model, *J. Geophys. Res.*, *115*, C06024, doi:10.1029/2009JC005591.

Wang, Y., B. Holt, W. E. Rogers, J. Thomson, and H. H. Shen (2016), Wind and wave influences on sea ice floe size and leads in the Beaufort and Chukchi Seas during the summer-fall transition 2014, *J. Geophys. Res. Oceans*, *121*, 1502–1525, doi:10.1002/2015JC011349.

Williams, T. D., L. G. Bennetts, V. A. Squire, D. Dumont, L. Bertino (2013a), Wave-ice interactions in the marginal ice zone. Part 1: Theoretical foundations, *Ocean Modell.*, *71*, 81–91, doi:10.1016/j.ocemod.2013.05.010.

Williams, T. D., L. G. Bennetts, V. A. Squire, D. Dumont, L. Bertino (2013b), Wave-ice interactions in the marginal ice zone. Part 2: Numerical implementation and sensitivity studies along 1D transects of the ocean surface, *Ocean Modell.*, *71*, 91–101, doi:10.1016/j.ocemod.2013.05.011.